

Chaos in Space and Time

Christopher Mehrvarzi, Mu Xu, Alireza Sedighi

Abstract— This paper introduces and addresses problems related to quantifying chaotic dynamics in both space and time. A wealth of research has been done to classify and quantify temporally chaotic systems. Traditional diagnostic tools such as Lyapunov exponents and vectors are extended to higher-dimensional problems that are common to spatially extended systems. We investigate the applications of these tools and the algorithms needed for calculation of higher dimensional systems. We employ these diagnostic tools to simplified numerical models: the one- and two-dimensional coupled map lattice and the Lorenz system of ordinary differential equations. The fractal dimension was calculated for the one- and two-dimensional coupled map lattices for different parameters. The fractal dimension was found to vary linearly with the system size which suggests extensive chaos. A method to calculate covariant Lyapunov vectors successfully captured the true perturbation growth in phase space. For the one-dimensional coupled map lattice, the hyperbolicity was not influenced much by system size. We extend our study to an experimentally relevant fluid convection system to gain insight on topical phenomena due to the presence of spatiotemporal chaotic behavior. Our investigation showed enhanced transport for a passive scalar species due to the presence of a spatiotemporally chaotic flow field. The transport enhancement factor was found ascribed to power laws similar to those found in experiments with different geometries and system sizes.

I. INTRODUCTION

The quantification and characterization of chaos in both space and time is at the forefront of dynamical systems research today. Systems with chaotic dynamics in time have been studied extensively since the phenomenon was first revealed by Lorenz (1963) in his seminal paper on atmospheric dynamics [1]. Many natural phenomena can be modeled as large, spatially-extended systems that exhibit complex dynamics in space. For example, these spatial complexities can be seen in the atmospheres of Earth and other planets, the dynamics of excitable media and the transport of biological species in ocean currents [2]. The study of systems with chaotic dynamics in both space and time is termed spatiotemporal chaos.

The quantification of systems exhibiting temporal chaos has relied on using tools and techniques in phase space; in particular, on the geometry of these objects in phase space to characterize these systems. To model spatiotemporal chaos, one must move from systems of ordinary differential equations to partial differential equations, which means a transition from finite dimensional systems to infinite dimensions in phase space. In this sense, characterizing spatiotemporal chaos

involves a transition away from the geometric descriptions that scientists and engineers have been familiar with for low dimensional systems.

The Lyapunov spectrum has been the method for characterizing chaotic systems. In this paper, the diagnostic tools used for quantifying temporal chaos will be extended to spatiotemporal systems using insights from simplified numerical models to solutions to governing partial differential equations. The Lyapunov spectrum will be calculated for simplified one- and two-dimensional coupled map lattice system, and the fractal dimension is determined for this system. Second, an overview of the algorithms developed for calculating the spectrum of Lyapunov exponents and covariant Lyapunov vectors will be presented and will be applied to the Lorenz system and discussed for high dimensional systems. Finally, solutions to the governing partial differential equations for a large-spatially extended system will be presented to connect theory with experimentally accessible results. One method for quantifying the transport of a passive scalar will be presented.

II. COUPLED MAP LATTICE

Coupled map lattices are simplified systems that provide important insight into certain physical phenomenon. These systems are also an excellent platform to study chaos in space and time. In this section, we will introduce Lyapunov diagnostic tools to one- and two-dimensional coupled map lattices.

A. Models

A coupled map lattice has discrete time, discrete space, and each lattice site has a continuous state [3]. Coupled map lattices take on many forms based on the type of coupling rule employed: additive, unidirectional, and diffusive coupling are three examples. In this study, the diffusive coupling rule is selected. One-dimensional and two-dimensional diffusive coupled map lattices can be described using equations 1 and 2, respectively:

$$x_i^{(n+1)} = f(x_i^n) + D\left[\frac{1}{2}(f(x_{i+1}^n) + f(x_{i-1}^n)) - f(x_i^n)\right], \quad (1)$$

$$x_{i,j}^{(n+1)} = f(x_{i,j}^n) + D\left[\frac{1}{4}(f(x_{i+1,j}^n) + f(x_{i-1,j}^n) + f(x_{i,j-1}^n) + f(x_{i,j+1}^n)) - f(x_{i,j}^n)\right]. \quad (2)$$

Here, i and j are lattice indexes, x is the lattice state, n is the time step, and D is the diffusion parameter. For these models, we chose random initial conditions and periodic boundary conditions. In addition, the logistic map is used as the mapping function which is defined as $f(x^n) = ax^n(1-x^n)$.

To calculate Lyapunov spectra of the model, it is necessary to linearize equations (1) and (2) as follows:

$$\delta x_i^{(n+1)} = f'(x_i^n) \delta x_i^{(n)} + D \left[\frac{1}{2} (f'(x_{i+1}^n) \delta x_{i+1}^{(n)} + f'(x_{i-1}^n) \delta x_{i-1}^{(n)}) - f'(x_i^n) \delta x_i^{(n)} \right], \quad (3)$$

$$\delta x_{i,j}^{(n+1)} = f'(x_{i,j}^n) \delta x_{i,j}^{(n)} + D \left[\frac{1}{2} (f'(x_{i+1,j}^n) \delta x_{i+1,j}^{(n)} + f'(x_{i-1,j}^n) \delta x_{i-1,j}^{(n)} + f'(x_{i,j+1}^n) \delta x_{i,j+1}^{(n)}) - f'(x_{i,j}^n) \delta x_{i,j}^{(n)} \right]. \quad (4)$$

The Gram-Schmidt reorthonormalization (GSR) approach is then used to reorthonormalize the vector computations [4]. In the first step, a set of orthogonal vectors are considered as initial ones $\{\delta x_1^1, \dots, \delta x_n^1\}$ or $\{\delta x_{1,1}^1, \dots, \delta x_{n,m}^1\}$, in which n and m are node numbers. In the next step, equations (1) and (3) or (2) and (4) are solved simultaneously to obtain the new set of vectors $\{\delta x_1^1, \dots, \delta x_n^1\}$ $\{\delta x_{1,1}^1, \dots, \delta x_{n,m}^1\}$. After each iteration of the algorithm, each vector will orient itself towards the direction of the vector of the maximum local growth [4]. To overcome this singularity, each vector is reorthogonalized after each step as follow:

$$\delta \bar{x}_1'(n) = \frac{\delta \bar{x}_1(n)}{\|\delta \bar{x}_1(n)\|}, \quad (5)$$

$$\delta \bar{x}_2'(n) = \frac{\delta \bar{x}_2(n) - \langle \delta \bar{x}_2(n), \delta \bar{x}_1'(n) \rangle \delta \bar{x}_1'(n)}{\left\| \delta \bar{x}_2(n) - \langle \delta \bar{x}_2(n), \delta \bar{x}_1'(n) \rangle \delta \bar{x}_1'(n) \right\|}, \quad (6)$$

⋮

$$\delta \bar{x}_n'(n) = \frac{\delta \bar{x}_n(n) - \langle \delta \bar{x}_n(n), \delta \bar{x}_{n-1}'(n) \rangle \delta \bar{x}_{n-1}'(n) - \dots - \langle \delta \bar{x}_n(n), \delta \bar{x}_1'(n) \rangle \delta \bar{x}_1'(n)}{\left\| \delta \bar{x}_n(n) - \langle \delta \bar{x}_n(n), \delta \bar{x}_{n-1}'(n) \rangle \delta \bar{x}_{n-1}'(n) - \dots - \langle \delta \bar{x}_n(n), \delta \bar{x}_1'(n) \rangle \delta \bar{x}_1'(n) \right\|}. \quad (7)$$

$\langle \cdot, \cdot \rangle$ is inner product. After n -normalization, the Lyapunov exponent can be calculated by equations (8-12):

$$\lambda_1^* = \lim_{n \rightarrow \infty} \frac{1}{n \Delta t} \sum_{i=1}^n \ln \|\delta \bar{x}_1(n)\|, \quad (8)$$

$$\delta \bar{x}_2^* = \delta \bar{x}_2(n) - \langle \delta \bar{x}_2(n), \delta \bar{x}_1'(n) \rangle \delta \bar{x}_1'(n), \quad (9)$$

$$\lambda_2^* = \lim_{n \rightarrow \infty} \frac{1}{n \Delta t} \sum_{i=1}^n \ln \|\delta \bar{x}_2^*\|, \quad (10)$$

⋮

$$\delta \bar{x}_n^* = \delta \bar{x}_n(n) - \langle \delta \bar{x}_n(n), \delta \bar{x}_{n-1}'(n) \rangle \delta \bar{x}_{n-1}'(n) - \dots - \langle \delta \bar{x}_n(n), \delta \bar{x}_1'(n) \rangle \delta \bar{x}_1'(n), \quad (11)$$

$$\lambda_n^* = \lim_{n \rightarrow \infty} \frac{1}{n \Delta t} \sum_{i=1}^n \ln \|\delta \bar{x}_n^*\|. \quad (12)$$

Finally, the fractal dimension will be obtained by using the Kaplan-Yorke formulation found in equation (7) [4]:

$$D_\lambda = j + \frac{\sum_{i=1}^j \lambda_i}{|\lambda_{j+1}|}. \quad (13)$$

Here, j is the index value that is defined by the constraints:

$$\sum_{i=1}^j \lambda_i > 0 \text{ and } \sum_{i=1}^{j+1} \lambda_i < 0. \quad (14)$$

B. The Lyapunov spectrum and fractal dimension for one-dimensional coupled map lattice

We simulate a one-dimensional coupled map lattice for a range of parameters. A model was simulated for 128 nodes with a diffusive coupling, $D=0.4$, and a logistic map parameter value, $a=3.7$. Figure 1 depicts Lyapunov spectrum for the results of this simulation. Since largest Lyapunov exponents are positive in magnitude, their summation will result in a positive slope as the lattice site increases, but as other Lyapunov exponents become negative, the slope of summation curve becomes negative and the sum decreases until the sum becomes negative. The point at which the sum crosses the zero summation line is defined as the fractal dimension, which is 47.807 for the selected parameters, as illustrated in Figure 1. It is known that for systems exhibiting chaotic behavior, this fractal dimension is a non-integer value. The relevance of this value is that it suggests the minimum number of dimensions or degrees

of freedom required to capture the important dynamics of the system.

Next, the dynamics of the coupled map lattice is studied as a function of the diffusion coupling coefficient. Figure 2 illustrates the variation of fractal dimension versus diffusion coefficient. We see that the increasing diffusion coefficient correlates to a decrease in the fractal dimension of the system. This makes sense physically since the diffusion coefficient is a dissipative parameter in the dynamical system and thus would reduce the size of the system and the number of relevant dynamical degrees of freedom.

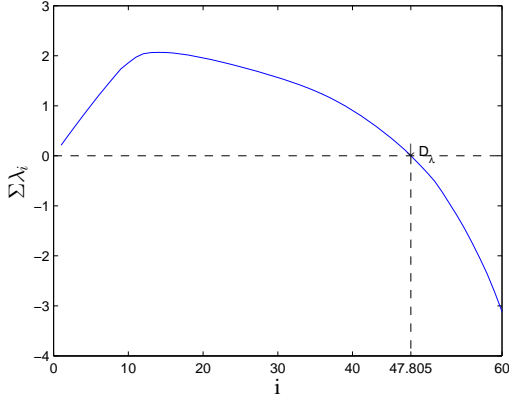


Figure 1: Lyapunov spectrum for $n = 128$, $D = 0.4$, and $a = 3.7$.

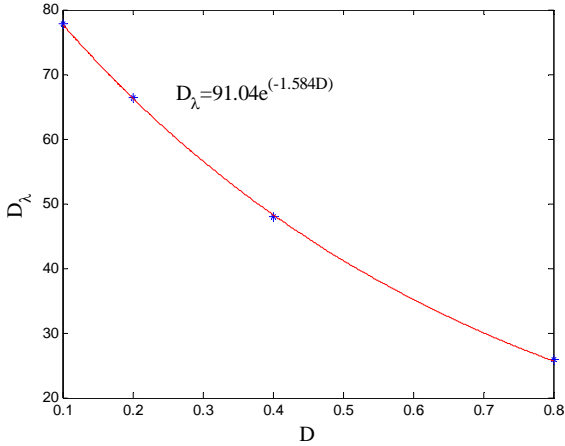


Figure 2: Plot of fractal dimension versus diffusion coefficient for $n = 128$ and $a = 3.7$.

C. The Lyapunov spectrum and fractal dimension for two-dimensional coupled map lattice

Many real-world examples can be modeled as a spatially extended, two-dimensional system that exhibit chaotic dynamics. These models have important implications in the prediction of weather, the spread of diseases and the modeling of other biological systems [6]. Therefore, the extension of Lyapunov diagnostic tools to a two-dimensional coupled map lattice is done to gain further physical insight. The Lyapunov spectrum

was calculated for a simulation of a two-dimensional coupled map lattice with a system size of 20×20 nodes, with parameters chosen to be $D = 0.4$ and $a = 3.7$. Figure 3 shows the power spectrum of the system. In this simulation, the fractal dimension is calculated to be 136.4047, which indicates that the number of relevant degrees of freedom is larger than the one-dimensional coupled map lattice which is expected from intuition. Figure 4 shows the color-plot of the lattice states for this coupled map lattice pattern. The aperiodicity of color pattern, as well as the fact that the patterns are larger than any individual lattice site, suggests spatially chaotic dynamics.

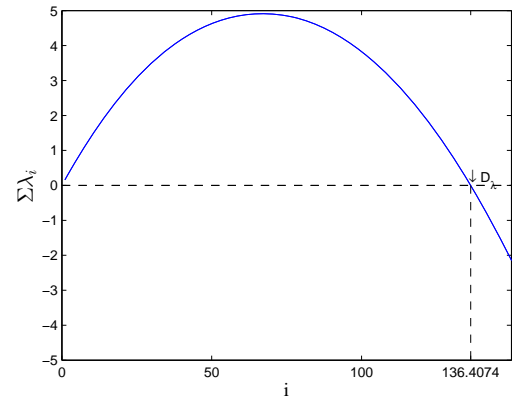


Figure 3: Lyapunov spectrum for $m \times n = 20 \times 20$, $D = 0.4$, and $a = 3.7$.

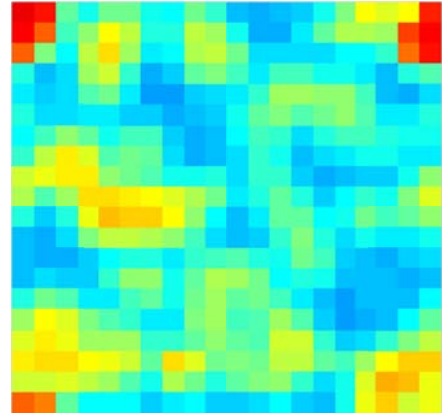


Figure 4: Pattern of two-dimensional coupled map lattice for $m \times n = 20 \times 20$, $D = 0.4$, and $a = 3.7$. The colors represent a spectrum of lattice states from 0 (blue) to 1 (red).

Spatiotemporal chaos should be extensive in the large system limit if

$$D_\lambda \propto \Gamma^d \quad (15)$$

where Γ is system size and d is the number of spatially extended dimensions. Then, in our case, $\Gamma = n$ and $d = 2$. To evaluate whether the system is extensive or

not, we simulate it for different coupled map lattice sizes. Figure 5 shows that the relationship between D_λ and n^2 is almost linear and therefore is characterized by extensive chaos. The slope of this line is represented by ξ_s and characterizes the chaotic length scale for the system and can be used to predict fractal dimensions of high-dimensional systems.

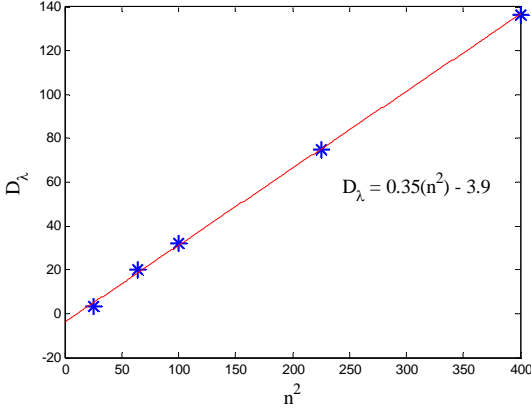


Figure 5: Plot of fractal dimension (D_λ) versus n^2 .

III. LYAPUNOV VECTOR

Lyapunov exponents are an important tool to quantifying the magnitude of a perturbation growth. In higher dimensional systems, it is useful to know the direction of this perturbation growth in phase space. One disadvantage to the method described in the previous section is the inability to extract this perturbation growth other than the leading order term. In this section, we will discuss one algorithm that can be used to calculate the covariant Lyapunov vectors to overcome this barrier.

A. Theoretical background

This section will highlight the use of covariant Lyapunov vectors as another method to quantify spatiotemporal chaos. The original idea comes from Oseledec (1968) [6]. In this paper the Oseledec Theorem was proposed which provides the theoretical background for Lyapunov exponents. His paper highlights two important conclusions for the study of covariant Lyapunov vectors. Theorem 1 states

$$A(\vec{x}_0) = \lim_{t \rightarrow \infty} [M^T(\vec{x}_0, t)M(\vec{x}_0, t)]^{\frac{1}{2t}} \quad (16)$$

where $M(\vec{x}_0, t)$ is the fundamental matrix that is defined by:

$$\dot{\vec{x}} = \vec{F}(\vec{x}), \quad (17)$$

$$J = \frac{\partial \vec{F}(\vec{x})}{\partial \vec{x}}, \quad (18)$$

and

$$\delta \vec{x}_t = M(\vec{x}_0, t) \delta \vec{x}_0. \quad (19)$$

J is the Jacobi matrix for the dynamical system. There are some important features for the fundamental matrix such as:

$$M(\vec{x}_0, t) \delta \vec{x}_0 = J_{t-1} J_{t-2} \cdots J_1 J_0, \quad (20)$$

$$\frac{d}{dt} M(\vec{x}_0, t) \delta \vec{x}_0 = J_t M(\vec{x}_0, t), \quad (21)$$

and

$$M(\vec{x}_0, 0) \delta \vec{x}_0 = I. \quad (22)$$

For the matrix $A(\vec{x}_0)$, the eigenvalues are the Lyapunov exponents. Theorem 2 states that

$$\lambda(\delta \vec{x}_0) = \lim_{t \rightarrow +\infty} \frac{1}{t} \ln (M(\vec{x}_0, t) \delta \vec{x}_0). \quad (23)$$

Theorem 1 proves the existence of Lyapunov exponents. Theorem 2 indicates some of the vectors are covariant with the dynamics of the system. If we apply the definition of Lyapunov exponents,

$$\lambda(\delta \vec{x}_0) = \lim_{t \rightarrow +\infty} \frac{1}{t} \ln \|\delta \vec{x}_t\| \quad (24)$$

to Theorem 2, we can prove:

$$\lambda(\delta \vec{x}_0 + \delta \vec{x}_0^*) \leq \max \{ \lambda(\delta \vec{x}_0) + \lambda(\delta \vec{x}_0^*) \} \quad (25)$$

where $\delta \vec{x}_0^*$ is a different initial vector of $\delta \vec{x}_0$. It indicates that from the combination of the initial conditions, we cannot extract any new Lyapunov exponents. There exists a set of special vectors, however, from which we can obtain all the Lyapunov exponents. These special vectors are linearly independent and are called covariant Lyapunov vectors. The algorithm used to calculate the covariant Lyapunov exponents is no different from the original method to calculate the Lyapunov exponents. The original algorithm of Lyapunov exponents is

$$\delta X^n = J_n Q^{n-1} \quad (26)$$

$$\delta X^n = Q^n R^n. \quad (27)$$

The δX^n is the matrix from the combination of $\delta \vec{x}_n$. Q^n and R^n are from QR-decomposition.

The algorithm of covariant Lyapunov vectors is [7]:

$$\delta X^{n+1} = J_n Q^n \quad (28)$$

$$\delta X^n = Q^n R^n. \quad (29)$$

The above process is the exact same as the original method, which is a forward iteration. Next, we need a backward iteration:

$$C^{n-1} = R^{n-1} C^n \quad (30)$$

$$V^{n-m} = Q^{n-m} C^{n-m}. \quad (31)$$

The initial condition for C^n can be chosen as a random up-triangle matrix. From the backward iteration process we can get C^{n-m} . The columns of matrix, V^{n-m} , are the covariant Lyapunov vectors at time $n-m$. The covariant Lyapunov vectors can reflect the true direction of perturbation growth or decay. So with covariant Lyapunov vectors, we can obtain more information about the perturbation field. From Lyapunov exponents, we can only get information about the magnitude of perturbation growth or decay; however, more physical insight can be gained from the direction of perturbation growth also.

B. The result from Lorenz system

The Lorenz system is a simplified system derived from the equations governing a Rayleigh-Bénard system. Since it is three-dimensional system, getting the covariant Lyapunov vectors is simpler than for higher dimensional systems. For this reason, it is an appropriate method for validating the algorithm to obtain covariant Lyapunov vectors. The Lorenz equations are:

$$\frac{dx}{dt} = \sigma(x - y) \quad (32)$$

$$\frac{dy}{dt} = x(\rho - z) - y \quad (33)$$

$$\frac{dz}{dt} = xy - \beta z. \quad (34)$$

The parameters chosen for our system are $\sigma=10$, $\rho=28$, and $\beta=\frac{8}{3}$ since these parameters guarantee chaotic dynamics and are used frequently in the literature. The phase portrait in the $x-z$ plane for the selected parameters is displayed in Figure 6.

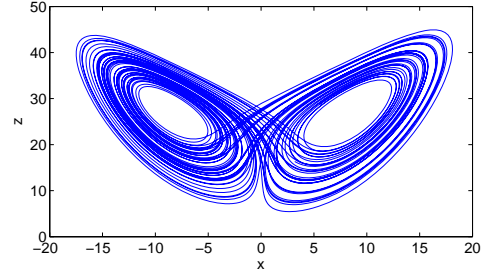


Figure 6: The phase portrait of the Lorenz equation in the $x-z$ plane for $\sigma = 10$, $\rho = 28$ and $\beta = 8/3$.

The Lyapunov exponents for the Lorenz system are calculated and displayed in Figure 7.

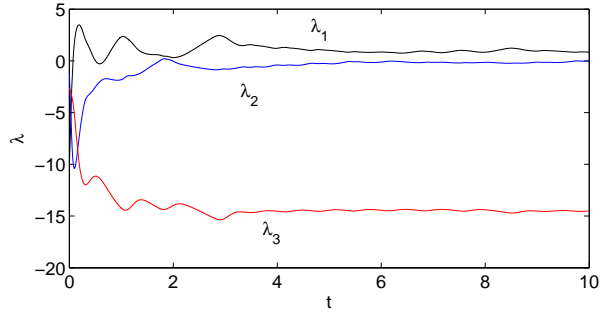


Figure 7: Plot of Lyapunov exponents in Lorenz system.

The covariant Lyapunov vector corresponding to the second order Lyapunov exponent should be parallel to the tangent vector. This is true because the tangent vector should be parallel to the Lyapunov vectors corresponding to a Lyapunov exponent equal to zero. This is shown in Figures 8 and 9.

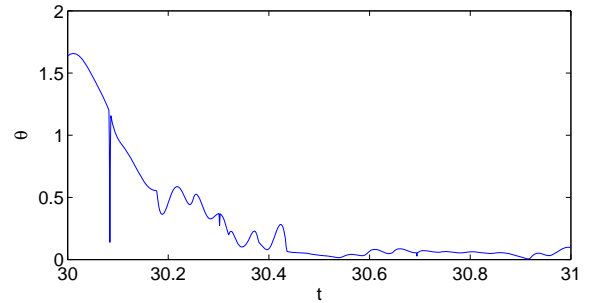


Figure 8: The angle between tangent vector and second order covariant Lyapunov vector.

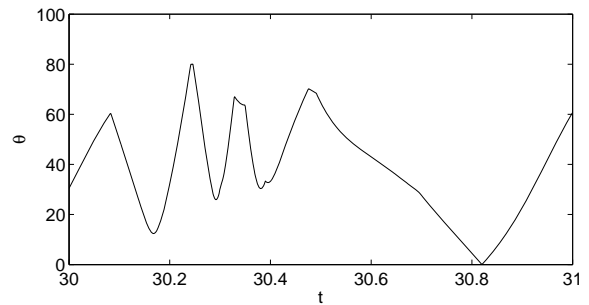


Figure 9: The angle between tangent vector and second order orthogonal Lyapunov vector.

Figure 8 is the angle between the second order covariant Lyapunov vector and the tangent vector. It is close to zero. Figure 9 is the angle between the second order orthogonal Lyapunov vector and the tangent vector. This angle does not converge to a single value.

C. The result of one-dimensional coupled map lattice

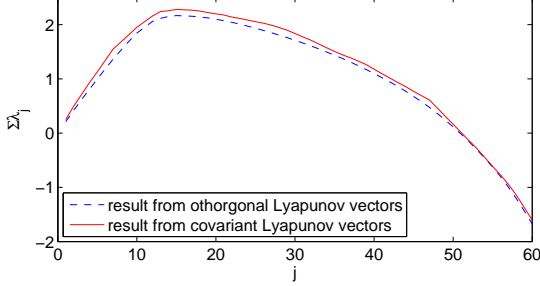


Figure 10: The result from 1D chain of diffusively coupled logistic maps.

In Figure 10, the dashed line is the summation of Lyapunov exponents which is calculated from the traditional algorithm for Lyapunov exponents. The solid line is the summation of Lyapunov exponents which is calculated from the covariant Lyapunov vectors. With the equation:

$$\lambda(\delta\vec{x}_0) = \frac{1}{t} \ln (M(\vec{x}_0, t)\delta\vec{x}_0) \quad (35)$$

the results from different algorithm are close agreement.

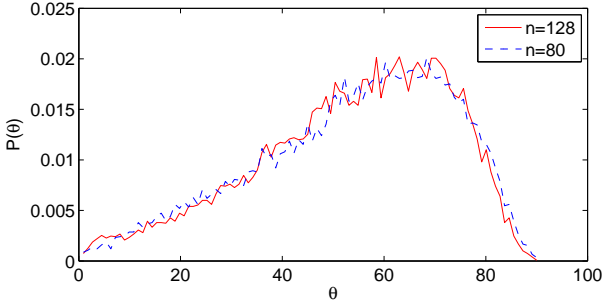


Figure 11: The principal angle between stable and unstable manifold.

Many theories are based on hyperbolic systems, however, in real world no such systems exist. In this case, evaluating the hyperbolicity of the system is important for establishing a theoretical framework. Because covariant Lyapunov vectors can reflect the direction of perturbation growth and decay, they can be used to evaluate the hyperbolicity of the system. The hyperbolicity of the system can be defined by the principal angle between the stable manifold and unstable manifold. In dynamical systems, the stable manifold is defined by the matrix of all the covariant Lyapunov vectors corresponding to the negative Lyapunov

exponents. The unstable manifold is defined by the matrix of all the covariant Lyapunov vectors corresponding to the positive Lyapunov exponents. For a pure hyperbolic system, the principal angle is 90 degrees. In Figure 11, the dashed line is the principal angle between the stable and unstable manifolds in the system with the number of lattice sites being 80. The solid line is the principal angle between the stable and unstable manifolds in the system where the number of lattice sites is 128. This implies that the scale of the system does not have significant influence on the principal angle.

IV. TRANSPORT IN A COMPLEX FLOW FIELD

The previous sections have discussed applying Lyapunov diagnostic tools to simplified models; however, these models do not reflect real-world systems accessible to experiment. We now extend this discussion to an experimentally relevant, infinite-dimensional fluid convection system governed by partial differential equations. The diagnostic tools used so far have been the crux of theoretical work to quantify chaotic systems, but these quantities cannot be measured in experiment. Alternative diagnostic tools that can be measured in experiment are proposed.

A. Boussinesq equations

The transport of a scalar species is an important phenomenon related to many areas of scientific and engineering interest and bridges the gap between spatiotemporal chaos theory and experiment [8]. Rayleigh-Bénard convection is the system that is selected to study transport due to extensive experimental work done on similar systems by which comparisons can be made [9,10]. The domain is heated from below and cooled from the top which creates a buoyancy-driven flow across the domain. A schematic of the domain is shown in Figure 12.

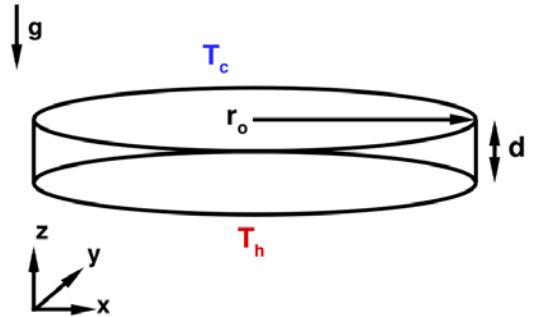


Figure 12: Rayleigh- Bénard convection cell.

The aspect ratio for this system is the ratio of the radius of the domain, r_0 , to the depth, d ,

$$\Gamma = \frac{r_0}{d}. \quad (36)$$

The boundary conditions used in the simulations are those that are accessible to experiment. The top and bottom of the domains were held at fixed temperatures with random thermal perturbations to break symmetry. Along the material walls no slip and conducting boundary conditions were imposed.

The partial differential equations governing the flow field dynamics are the Boussinesq equations:

$$\sigma^{-1}(\partial_t + \bar{\mathbf{u}} \cdot \bar{\nabla})\bar{\mathbf{u}} = -\bar{\nabla}p + \bar{\nabla}^2\bar{\mathbf{u}} + RT\hat{\mathbf{z}} \quad (37)$$

$$(\partial_t + \bar{\mathbf{u}} \cdot \bar{\nabla})T = \bar{\nabla}^2T \quad (38)$$

$$\bar{\nabla} \cdot \bar{\mathbf{u}} = 0 \quad (39)$$

where the flow field is defined by the velocity, $u(x, y, z, t)$, the temperature, $T(x, y, z, t)$, and the pressure, $p(x, y, z, t)$ fields and σ is the Prandtl number. The equations are non-dimensionalized by the vertical thermal diffusion time d^2/α where α is the thermal diffusivity.

The Rayleigh number, R , is the non-dimensional measure of the temperature difference across the domain. It is defined as

$$R = \frac{\alpha g \Delta T d^3}{\nu \kappa} \quad (40)$$

and is a measure of the ratio of the buoyancy to viscous forces. For the cylindrical domain that is investigated, the onset of convection occurs at a critical Rayleigh number of about $R_c \approx 1708$. When the Rayleigh number is increased further, defects begin to develop in the convection roll pattern until a time-dependent pattern in the flow field emerges and the onset of spatiotemporal chaos occurs.

Figure 13 shows a typical mid-plane solution to the Boussinesq equations at a Rayleigh number where the flow field is spatiotemporally chaotic.

B. Advection-diffusion equation

The transport of passive scalar species is described by the advection-diffusion equation

$$(\partial_t + \bar{\mathbf{u}} \cdot \bar{\nabla})c = L\bar{\nabla}^2c \quad (41)$$

where $c(x, y, z, t)$ is the concentration field, and the L

is the Lewis number which is the $L = D/\alpha$, where D is the molecular diffusivity. In this study, Lewis numbers of $10^{-3} < L < 10^{-1}$ are explored since these values are experimentally accessible and are relevant to the results presented in the literature [7, 8].

C. Numerical scheme

A spectral element scheme is used to solve the Boussinesq and advection-diffusion equations simultaneously. The numerical scheme is second or third order accurate in time and exponentially convergent in space. The stability criteria is dictated by the spatial step

$$\Delta x \approx \left(\frac{L}{\|\bar{\mathbf{u}}\|} \right)^{1/2} \quad (42)$$

The small Lewis numbers that are studied are computationally accessible using a filtering procedure described in more detail by Chiam (2005) [11]. More details about the general numerical scheme can be found in Fisher (1997) [12].

D. Results

A typical flow field from solving the Boussinesq equations at a Rayleigh number of 6000 is depicted in Figure 13.

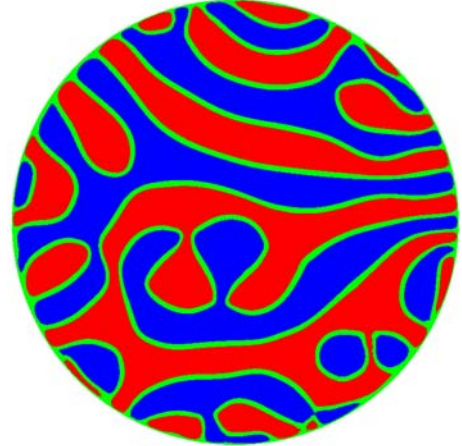


Figure 13: Rayleigh- Bénard convection flow field at $R = 6000$. The red indicates hot rising fluid and the blue is cold sinking fluid.

The flow field was allowed to develop for 50 time units before the passive scalar was placed. An initial Gaussian distribution was placed in the flow field and solved simultaneously. The images that are found in Figure 14 below show important qualitative features about the evolution of the passive scalar field as a function of the Lewis number. We see that transport of the species is inhibited when the Lewis number is smaller as seen in the images in (c) in Figure 14. In other

words, the concentration of the species is localized in these cases. We also see transport occurring normal to roll boundaries as seen in images in (a) of Figure 14, but transition occurring to transport parallel to the roll boundaries as the Lewis number decreases. This observation has been seen and quantified in simulations of similar systems [11].

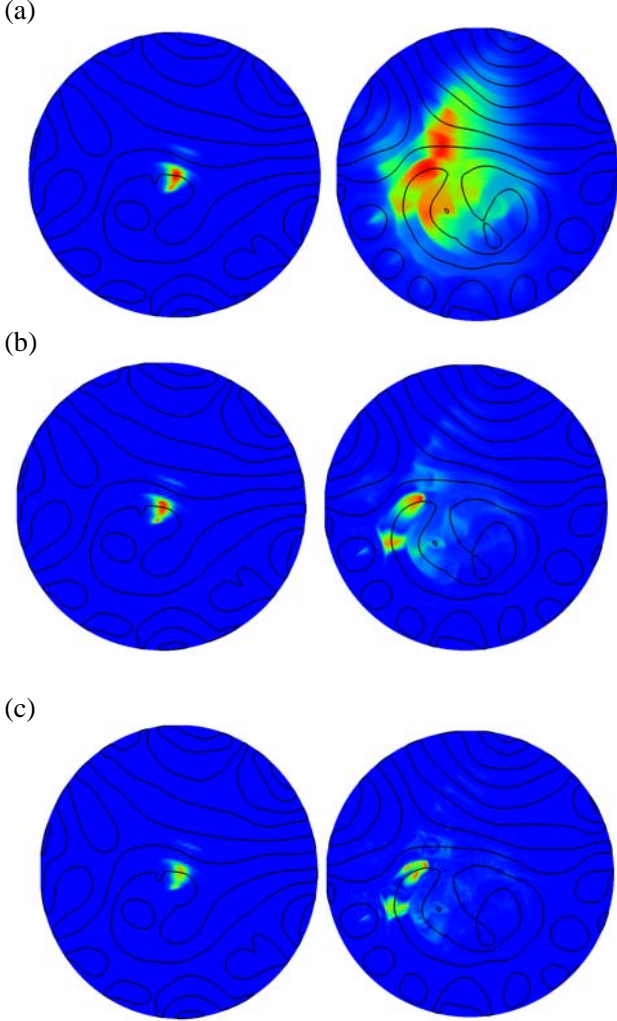


Figure 14: Evolution of the passive scalar distributions after six time units for a range of Lewis numbers: (a) $L=10^{-1}$ (b) $L=10^{-2}$ and (c) $L=10^{-3}$. The black contour lines indicate mid-plane temperature values and the pseudo-color represent concentration of the passive scalar concentration (red is highest concentration, blue is lowest concentration).

One way to quantify the transport of the passive scalar is to look at the statistics of the spreading of the species concentration. Our analysis of the spreading can be reduced to two dimensions due to the spatially extended convection cell system that is studied. The mean-square displacement is defined as

$$V(t) = \frac{\int_0^{\Gamma} \int_0^{2\pi} [r - \bar{r}(t)]^2 c(r, \theta, t) r dr d\theta}{\int_0^{\Gamma} \int_0^{2\pi} c(r, \theta, t) r dr d\theta} \quad (43)$$

where the quantity $\bar{r}(t)$ is the center of mass of the tracer concentration field and is defined as

$$\bar{r}(t) = \frac{\int_0^{\Gamma} \int_0^{2\pi} r c(r, \theta, t) r dr d\theta}{\int_0^{\Gamma} \int_0^{2\pi} c(r, \theta, t) r dr d\theta} \quad (44)$$

The mean-square displacement is calculated over time for each of the simulations ran. Figure 15 shows mean-square displacement as a function of time for the cases of $R=3000$ and $R=6000$. The results show that the mean-square displacement grew proportionally with a power law of unity. This proportional growth suggests that the spreading of the averaged passive scalar concentration field, $\tilde{c}(r, t)$ is a normal diffusive process that can be described by a reduced one-dimensional diffusive process governed by,

$$\partial_t \tilde{c} = L^* \nabla^2 \tilde{c} \quad (45)$$

where L^* is the effective Lewis number and is extracted from the mean-square displacement by the expression

$$V(t) = 4L^* \partial_{rr} \tilde{c} \quad (46)$$

Another test that can be done to confirm the averaged spreading as a normal diffusive process is to look at ratios of higher order moments to the mean-square displacement. For normal diffusive processes, the ratio should scale

$$\frac{V_q(t)^{2/q}}{V(t)} = const \quad (47)$$

where q is an integer of higher order moments. Plotted in Figure 16 are the ratios with higher order moments of $q=4, 6$ and 8 . The values approaching a constant value over time confirm a normal diffusion process.

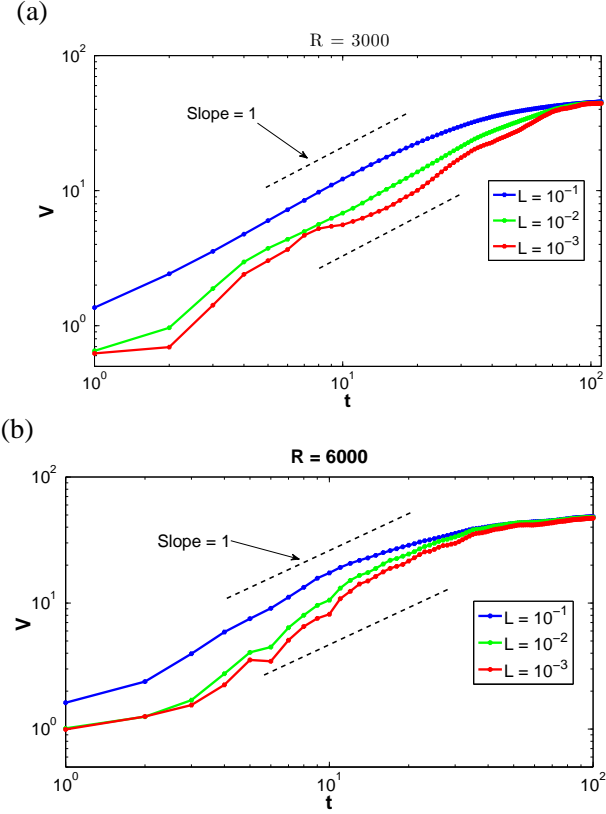


Figure 15: Plots of the mean-square displacement of the passive scalar concentration for (a) $R = 3000$ and (b) $R = 6000$. The spreading is compared with a slope of unity that is defined by an overall normal diffusive process.

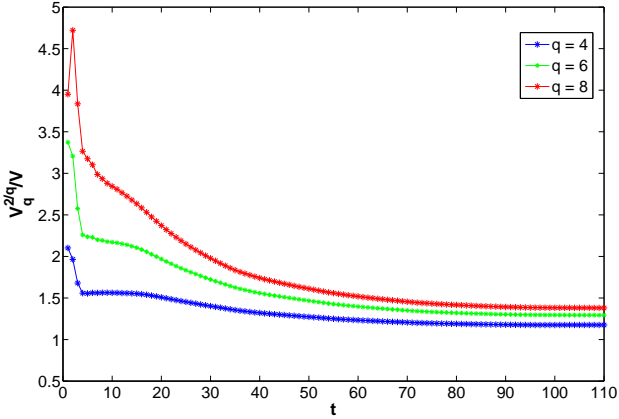


Figure 16: Plot of the ratio of higher order moments to the mean-square displacement as a function of time. Higher order moments of $q = 4, 6,$ and 8 are color differentiated.

Using the enhanced Lewis number, a transport enhancement factor due to the presence of the spatiotemporally chaotic flow field is defined to be

$$\Delta = \frac{L^* - L}{L} \quad (48)$$

It is desirable to see how the transport enhancement factor trends as a function of the characteristic velocity of the flow field, so it is compared with the Péclet number which is defined as

$$P = \frac{\|\bar{u}\|}{L} \quad (49)$$

where the characteristic velocity magnitude, $\|\bar{u}\|$, is calculated from the maximum value of the velocity in the flow field. The transport enhancement feature as a function of the Péclet number is shown in Figure 17. Two regimes emerge in this transport enhancement plot: a low Péclet number regime defined as diffusive-dominated transport and a high Péclet number regime defined as advection-dominated transport. In diffusive-dominated systems, the transport enhancement factor scales with $P^{1/2}$ and in advection-dominated systems, the transport enhancement factor scales with P^1 . These trends are validated by similar ones seen in experimental work done by Solomon and Gollub in a rectangular domain of Rayleigh-Bénard convection [9, 10].

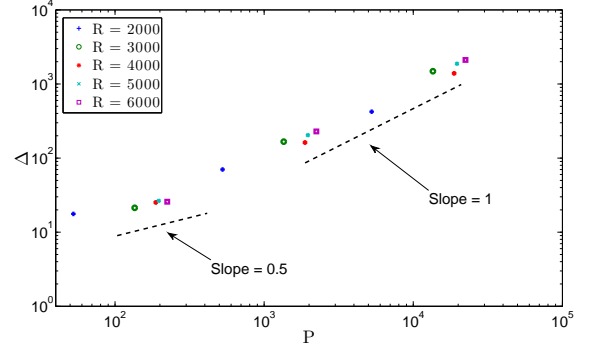


Figure 17: Plot of the transport enhancement factor as a function of the Péclet number for the range of Rayleigh numbers that were tested. The low Péclet number regime is compared with a slope of 0.5 and the high Péclet number regime is compared with a slope of unity.

From the trends seen in Figure 17, one would expect the effective Lewis number to scale proportionally with the characteristic velocity in the high Péclet number regime. This can also be seen by multiplying equations (48) and (49) by the Lewis number to obtain

$$L^* - L \propto \|\bar{u}\|. \quad (50)$$

Figure 18 plots the enhanced Lewis number as a function of the reduced Rayleigh number,

$$\varepsilon = \frac{R - R_c}{R_c} \quad (51)$$

which shows that the enhanced Lewis number scales with the Péclet number to the 0.5 power.

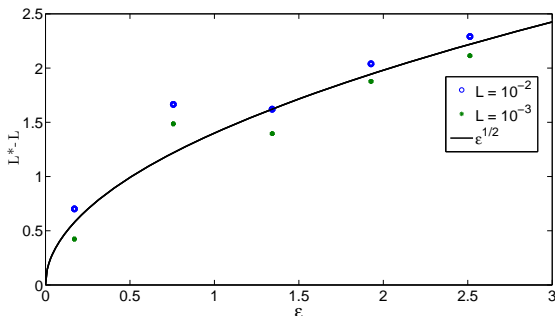


Figure 18: Plot of the effective Lewis number as a function of the reduced Rayleigh number. Figure shows that for advection-dominated transport, the effective Lewis number scales with the Péclet number to the 0.5 power.

V. CONCLUSION

In this paper, we explore spatiotemporal chaos using simple numerical models which are important to the study of many natural phenomena including thermal-fluid systems, neural networks, pattern formation in nature, and population dynamics. In our study, we applied diagnostic tools like the Lyapunov spectrum and the fractal dimension to quantify the chaotic dynamics for a one- and two-dimensional coupled map lattices. This study showed that the fractal dimension scaled with the map lattice size which indicates extensive chaos. In some systems, however, the true direction of the all the perturbation growths are required and other methods must be applied. To amend this shortcoming, we discussed and implemented an algorithm for calculating the covariant Lyapunov vectors which preserves the true direction in phase space, and thus reflects the direction of perturbation. The algorithm was validated on the one-dimensional coupled map lattice, the results of which showed good agreement between the two methods. Additionally, the hyperbolicity of this lattice map was calculated and was found to not be influenced by the size of the map significantly.

Finally, we investigated a large spatially-extended fluid convection system exhibiting spatiotemporal chaos with experimentally relevant boundary conditions. Tools to quantify the transport of a passive scalar were presented and results showed that the transport of the species followed power laws similar to those found in experimental systems of different sizes and geometries.

For future work, we would like to implement the algorithm discussed in Section III for calculating the covariant Lyapunov vectors to the experimentally relevant Rayleigh-Bénard convection. A formal study

into the effect of system size on the results obtained in this paper is also desired. Pursuing this work could lead to novel insights into pattern formation in large, natural systems exhibiting spatiotemporal chaos.

REFERENCE

- [1] Lorenz, Edward N. "Deterministic nonperiodic flow." *Journal of the Atmospheric Sciences* 20.2 (1963): 130-141.
- [2] Falkowski, Paul. "Ocean Science: The power of plankton." *Nature* 483.7387 (2012): S17-S20.
- [3] Kaneko, K. "Lyapunov analysis and information flow in coupled map lattices." *Physica D: Nonlinear Phenomena* 23 (1986) : 436-447.
- [4] Wolf, A., Swift B. J., Swinney, L. H., Vastano, J. A. "Determining Lyapunov exponents from a time series." *Physica D: Nonlinear Phenomena* 16 (1985) : 285-317.
- [5] Primo, C., Szendro, I. G., Rodríguez, M. A., Gutiérrez, J. M. "Error growth patterns in systems with spatial chaos: From coupled map lattices to global weather models." *Physical Review Letters* 98.10 (2007): 108501.
- [6] Oseledec, V. I. "A multiplicative ergodic theorem. Lyapunov characteristic numbers for dynamical systems." *Transactions of the Moscow Mathematical Society* 19.2 (1968): 197.
- [7] Ginelli, F., Poggi, P., Turchi, A., Chaté, H., Livi, R., Politi, A., "Characterizing Dynamics with Covariant Lyapunov Vectors." *Physical Review Letters* 99.13 (2007): 130601.
- [8] Gollub, J. P., and M. C. Cross. "Nonlinear dynamics: Chaos in space and time." *Nature* 404.6779 (2000): 710-711.
- [9] Solomon, T. H., and J. P. Gollub. "Passive transport in steady Rayleigh-Bénard convection." *Physics of Fluids* 31 (1988): 1372.
- [10] Solomon, T. H., and J. P. Gollub. "Chaotic particle transport in time-dependent Rayleigh-Benard convection." *Physical Review A* 38.12 (1988): 6280.
- [11] Chiam, K. H., Cross, M. C., Greenside, H. S., Fischer, P. F., "Enhanced tracer transport by the spiral defect chaos state of a convecting fluid." *Physical Review E* 71.3 (2005): 036-205.
- [12] Fischer, Paul F. "An overlapping Schwarz method for spectral element solution of the incompressible Navier-Stokes equations." *Journal of Computational Physics* 133.1 (1997): 84-101.